The stellar and dark matter distributions in elliptical galaxies from the ensemble of strong gravitational lenses

Masamune Oguri,[1,2]* Cristian E. Rusu[3,4] and Emilio E. Falco[5]

[1] *Department of Physics, University of Tokyo, 7-3-1 Hongo, Bunkyo-ku, Tokyo 113-0033, Japan*
[2] *Kavli Institute for the Physics and Mathematics of the Universe (Kavli IPMU, WPI), University of Tokyo, Chiba 277-8583, Japan*
[3] *Optical and Infrared Astronomy Division, National Astronomical Observatory of Japan, 2-21-1 Osawa, Mitaka, Tokyo 181-8588, Japan*
[4] *Department of Astronomy, University of Tokyo, 7-3-1 Hongo, Bunkyo-ku, Tokyo 113-0033, Japan*
[5] *Harvard-Smithsonian Center for Astrophysics, Whipple Observatory, 670 Mt. Hopkins Road, P.O. Box 6369, Amado, AZ 85645, USA*

24 September 2013

ABSTRACT

We derive the average mass profile of elliptical galaxies from the ensemble of 161 strong gravitational lens systems selected from several surveys, assuming that the mass profile scales with the stellar mass and effective radius of each lensing galaxy. The total mass profile is well fitted by a power-law $\rho(r) \propto r^{\gamma}$ with best-fit slope $\gamma = -2.11 \pm 0.05$. The decomposition of the total mass profile into stellar and dark matter distributions is difficult due to a fundamental degeneracy between the stellar initial mass function (IMF) and the dark matter fraction f_{DM}. We demonstrate that this IMF-f_{DM} degeneracy can be broken by adding direct stellar mass fraction measurements by quasar microlensing observations. Our best-fit model prefers the Salpeter IMF over the Chabrier IMF, and a smaller central dark matter fraction than that predicted by adiabatic contraction models.

Key words: dark matter — galaxies: elliptical and lenticular, cD — galaxies: formation — galaxies: haloes — gravitational lensing: strong

1 INTRODUCTION

The standard collisionless cold dark matter model predicts that the density profile of dark matter haloes is universal (Navarro, Frenk, & White 1997, hereafter NFW). In observations, the radial density profile of dark haloes has been tested well in clusters of galaxies using gravitational lensing. The results indicate that the observed radial profiles agrees very well with the NFW profile from cluster cores out to virial radii (e.g., Mandelbaum et al. 2006; Johnston et al. 2007; Umetsu et al. 2011; Oguri et al. 2012a; Newman et al. 2013a; Okabe et al. 2013).

On the other hand, studies of dark matter density profiles for galaxy-scale haloes are more complicated because of the larger effects of central galaxies. While stacked weak lensing has shown that the average radial density profile of galaxy-scale haloes is consistent with the NFW profile (e.g., Hoekstra, Yee, & Gladders 2004; Gavazzi et al. 2007; Mandelbaum, Seljak, & Hirata 2008; Leauthaud et al. 2012), the inner density profile is significantly steeper than the NFW profile due to the dominant contribution of the baryonic matter near the galaxy centre. For example, the central density profiles of massive elliptical galaxies have

been extensively studied using velocity dispersion measurements (see Binney & Tremaine 2008) and strong gravitational lensing (see Treu 2010), which indicates that the total mass profile of elliptical galaxies are nearly isothermal with the radial density profile $\rho(r) \propto r^{-2}$.

The stellar kinematics provide a powerful means of studying the mass profile of the core of galaxies. In particular, recent systematics observations with integral field spectroscopy, such as SAURON (Bacon et al. 2001; Cappellari et al. 2006, 2007; Kuntschner et al. 2010) and ATLAS[3D] (Cappellari et al. 2011, 2013a,b; Krajnović et al. 2011), has revealed detailed internal structures of elliptical galaxies. A complication in the interpretation of the kinematics data, however, is the orbital anisotropy which degenerates with the mass estimate from stellar kinematics data.

Strong gravitational lensing robustly measures the projected mass enclosed by the Einstein radius, and therefore provides a powerful alternative to measuring the mass distribution in the cores of elliptical galaxies. While strong lensing of single background sources alone does not constrain the radial density profile of individual lensing galaxies very well, the combination of strong lensing and stellar kinematics is powerful in measuring the radial density slope, because these two probes constrain enclosed masses at different radii (Treu & Koopmans 2002, 2004). The power of

* E-mail: masamune.oguri@ipmu.jp

this approach has been well demonstrated by the Sloan Lens ACS Survey (SLACS; Bolton et al. 2006, 2008a; Auger et al. 2009; Koopmans et al. 2009), the Sloan WFC Edge-on Late-type Lens Survey (SWELLS; Treu et al. 2011; Dutton et al. 2013), and the BOSS Emission-Line Lens Survey (BELLS; Brownstein et al. 2012; Bolton et al. 2012). Again, one of the major systematic uncertainties inherent in this combined analysis is the orbital anisotropy.

In this paper, we constrain the average mass distribution of elliptical galaxies from the statistical analysis of a large sample of strong gravitational lenses. Our approach is essentially similar to the one proposed in Rusin, Kochanek, & Keeton (2003) and Rusin & Kochanek (2005) in which a self-similar model of stellar and dark matter distributions is assumed to describe various strong lens systems with different lens masses and Einstein radii (see also Ferreras, Saha, & Williams 2005; Bolton et al. 2008b; Grillo 2010, 2012). We extend the analysis by using galaxy-galaxy strong lenses from SLACS and BELLS as well as strongly lensed quasars, resulting in a sample of 161 strong gravitational lenses in total. This approach relies only on gravitational lensing, and therefore is immune to the orbital anisotropy.

When combining strong lenses with different masses of lensing galaxies, we rescale the masses with stellar mass measurements of individual lensing galaxies. However, the stellar mass estimate is subject to various uncertainties, most notably the uncertainty from the stellar initial mass function (IMF; Salpeter 1955; Kroupa 2001; Chabrier 2003) such that estimated stellar masses depend strongly on the assumed functional form of the IMF. Once this uncertainty is taken into account, stellar and dark matter distributions are highly degenerate. We break this degeneracy using quasar microlensing (see Wambsganss 2006) which directly probes the stellar mass fraction at the positions of quasar images.

This paper is organised as follows. In Section 2 we present our strong lens sample. We conduct a statistical analysis in Section 3, and discuss implications for the adiabatic contraction in Section 4. Finally we summarize our results in Section 5. Throughout this paper we assume a flat universe with matter density $\Omega_M = 0.3$, cosmological constant $\Omega_\Lambda = 0.7$, and Hubble constant $H_0 = 70\,\mathrm{km\,s^{-1}Mpc^{-1}}$.

2 LENS SAMPLE

2.1 Strong Lenses

Here we describe a sample of strong lenses used for our statistical analysis. We use strong lenses discovered in various surveys. Our sample includes both galaxy-galaxy quasar-galaxy lenses.

We use the SLACS galaxy-galaxy strong lens sample from Auger et al. (2009), in which multi-band *Hubble Space Telescope (HST)* imaging results of the full SLACS lens sample were presented. Among the 85 grade "A" systems presented in Auger et al. (2009), we select a subsample of 70 lens systems based on the availability of multi-band images for the stellar mass estimate (see below) and the Einstein radius measurement. Most of the lenses were observed in

V- and *I*-band, and some of them were observed in *B*- or *H*-band as well. The effective radius of each lensing galaxy measured in *I*-band was also presented. Based on the arguments in Auger et al. (2009), we assume conservative 5% errors on the effective radii. The Einstein radii are derived from mass modelling assuming the Singular Isothermal Ellipsoid (SIE) model (Bolton et al. 2008a).

In addition, we include a galaxy-galaxy strong lens sample from BELLS (Brownstein et al. 2012). We use all 25 definite lens systems, for which the effective radius measurement from *HST I*-band imaging data is available. We assign 10% errors to the effective radii (see Brownstein et al. 2012). The Einstein radius for each lens system was obtained again by fitting the lensed galaxy assuming the SIE model for the mass distribution.

We use a sample of strongly lensed quasars compiled in the CASTLES webpage[1]. Most of the CASTLES quasar lenses were observed in *HST V*-, *I*-, and *H*-bands. We measure the effective radius (and its error) of each lensing galaxy using the *H*-band image, or *I*-band image if the *H*-band image is not available. We select a subsample of 38 quasar lenses from the CASTLES based on the following criteria. First, both the source and lens redshifts must be measured in order to convert the Einstein radius to the enclosed mass. Second, we exclude complex lens systems such as lensing by multiple galaxies and lensing by a cluster of galaxies. Third, we exclude lensing galaxies with dominant disk components, except for Q2273+0305 which is produced by a massive bulge of a spiral galaxy. Finally we set the condition that the effective radius of the lensing galaxy must be measured with a small uncertainty. We also include COS-MOS5921+0638 (Anguita et al. 2009) which is not in our CASTLES quasar lens list but has an *HST* image for accurate astrometry and galaxy profile measurement. The resulting subsample contains 38 quasar lenses. For each lens system we perform mass modelling using *glafic* (Oguri 2010). We assume the SIE model plus external shear, with priors on the ellipticity and position angle of the SIE component from the measured galaxy light profile. We derive the Einstein radius for each lens system from the best-fitting model.

The Sloan Digital Sky Survey Quasar Lens Search (SQLS; Oguri et al. 2006, 2008, 2012b; Inada et al. 2008, 2010, 2012) has identified nearly 50 new quasar lens systems from the Sloan Digital Sky Survey (SDSS) data[2]. We are conducting a large programme to observe the new SQLS lens systems (Rusu et al. 2011; C. E. Rusu et al., in preparation) using the Laser Guide Star Adaptive Optics (LGSAO) system at the Subaru telescope (Hayano et al. 2008, 2010). Among about 20 quasar lens systems we have already observed with the Subaru LGSAO, we select a subsample of 7 quasar lenses based on the same criteria as used for the CASTLES sample. The subsample includes SDSSJ0806+2006 which was in fact observed with the Very Large Telescope LGSAO system (Sluse et al. 2008). Our careful analysis of the Subaru LGSAO images demonstrates that accurate and robust estimates of galaxy morphology parameters such as the effective radius and Sersic index are indeed feasible (C. E. Rusu et al., in preparation). We derive the measurement

---

[1] http://cfa-www.harvard.edu/castles/
[2] http://www-utap.phys.s.u-tokyo.ac.jp/~sdss/sqls/

error of the effective radius for each lens system by marginalising over PSF uncertainties. Again, the Einstein radius for each lens system is based on mass modelling using *glafic* (Oguri 2010) assuming the SIE profile.

The CFHTLS Strong Lensing Legacy Survey (SL2S; Cabanac et al. 2007; Ruff et al. 2011; More et al. 2012; Gavazzi et al. 2012) constructed a large sample of galaxy-galaxy strong lenses identified from the Canada-France-Hawaii Telescope Legacy Survey (CFHTLS). Sonnenfeld et al. (2013a,b) presented *HST* imaging results and spectroscopic follow-up results for the final sample of the SL2S galaxy-scale strong lenses. Among the 56 strong lens candidates presented in Sonnenfeld et al. (2013a,b) we select a subsample of 21 lens systems based on the availability of *HST* images for determining galaxy morphology parameters as well as spectroscopic redshifts of both the lens and source. The error on the effective radius is conservatively assumed to be 10%. Sonnenfeld et al. (2013a) also provided the Einstein radii derived assuming the SIE profile.

2.2 Stellar Mass Estimate

We derive the stellar mass of each lensing galaxy by fitting the observed spectral energy distribution (SED) to a stellar population synthesis (SPS) model. Specifically, we use the SPS model of Bruzual & Charlot (2003). For simplicity, we adopt a single burst model with the metallicity and formation redshift as parameters. We include a Gaussian prior on the metallicity with a mean $Z = 0.01$ and standard deviation 0.14 dex for the initial stellar mass of $10^{11} M_\odot$. We include the stellar mass dependence of the mean as $Z \propto M_*^{0.15}$. In addition, we include a Gaussian prior on the formation redshift with a mean 2 and standard deviation 0.5. The wavelength bands for the SED fitting differ for different lens systems, but we typically use *HST V*-, *I*-, and *H*-band images for the SLACS sample, *HST I*-band and SDSS *griz*-band images for the BELLS sample, *HST V*-, *I*-, and *H*-band images for the CASTLES sample, non-AO *I*- and AO *K'*-band images for the SQLS+AO sample, and *HST V*-band CFHTLS *griz*-band images for the SL2S sample. In order to accommodate the model uncertainty, we set a minimum magnitude error of 0.1 for each band. We assume the Salpeter IMF to derive the stellar mass, but in our analysis below we fully take account of the IMF uncertainty.

We check the validity of our stellar mass estimate by comparing our result with stellar masses derived in Auger et al. (2009). They also used he SPS model of Bruzual & Charlot (2003), but considered a more complex star formation history. We find that our stellar mass estimate is in good agreement with that of Auger et al. (2009) for the same Salpeter IMF case. More quantitatively, differences of $\log M_*^{\rm Sal}$ between our estimates and those of Auger et al. (2009) has a mean -0.02 and standard deviation 0.03, with no clear dependence of the difference on the stellar mass.

Figure 1 shows the stellar mass and lens redshifts for the strong lens sample. The stellar masses are in the relatively narrow range of $10^{11} M_\odot \lesssim M_*^{\rm Sal} \lesssim 10^{12} M_\odot$, and the lens redshifts are broadly distributed up to $z_l \sim 1$. The list of all the strong lens systems is in Appendix A.
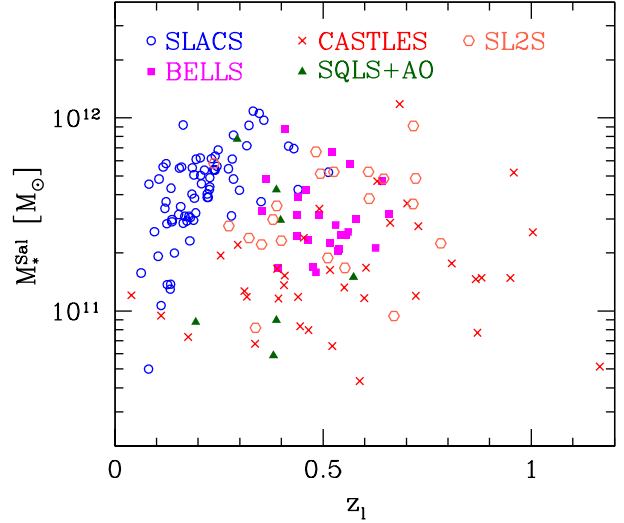

Figure 1. Redshifts z_l and stellar masses $M_*^{\rm Sal}$ derived assuming the Salpeter IMF for lensing galaxies of the strong lens sample used in our statistical analysis. Different symbols show lens samples from different surveys.

3 STATISTICAL ANALYSIS

3.1 Total Mass Distribution

We constrain the average total mass profile for our strong lens sample assuming that the profile scales with the stellar mass and effective radius of the lensing galaxy. Specifically, for each strong lens system we compute the scaled projected mass $M_{\rm tot}(< R_{\rm Ein})/M_*^{\rm Sal}$, where $M_{\rm tot}(< R_{\rm Ein})$ is the total projected mass enclosed by the Einstein radius $R_{\rm Ein} = D_{\rm A}(z_l)\theta_{\rm Ein}$. We compute $M_{\rm tot}(< R_{\rm Ein})$ from the Einstein radius via $M_{\rm tot}(< R_{\rm Ein}) = \pi R_{\rm Ein}^2 \Sigma_{\rm cr}$ with $\Sigma_{\rm cr}$ being the critical surface mass density. By combining scaled projected mass measurements for different strong lens systems, we can reconstruct the scaled projected mass profile, $M_{\rm tot}(< R)/M_*^{\rm Sal}$, as a function of the projected radius normalized by the effective radius, R/R_e (Rusin, Kochanek, & Keeton 2003; Rusin & Kochanek 2005).

We assume an error of 10% for the stellar mass estimate for the SLACS, CASTLES, and SQLS+AO samples, and a larger error of 20% for the BELLS and SL2S samples given the lack of high-resolution near-infrared images. The assumed model error of the stellar masses for the SLACS sample is comparable to the one estimated in Auger et al. (2009). The measurement error of the effective radius R_e is propagated to the error on the total projected mass assuming $M_{\rm tot}(< R) \propto R$, which will be shown to be reasonable in our analysis below. We neglect the error on the Einstein radius because it is usually much smaller compared with errors on the stellar mass and effective radius.

Figure 2 shows projected mass measurements for our sample of strong lenses. There is a clear trend that the scaled projected mass is roughly proportional to the projected radius. We fit the trend with a self-similar power-law mass model of the following form:

$$\frac{M_{\rm tot}(< R)}{M_*^{\rm Sal}} = A \left(\frac{R}{R_e}\right)^{3+\gamma}, \tag{1}$$

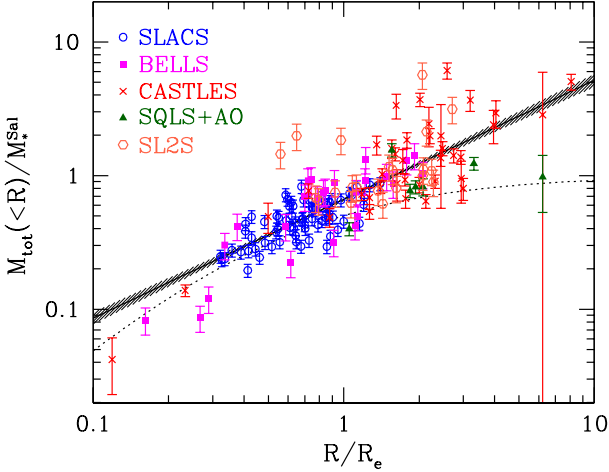where γ is the radial slope of the three-dimensional density

Figure 2. The scaled projected mass, $M_{\rm tot}(< R)/M_*^{\rm Sal}$, as a function of the projected radius normalized by the effective radius, R/R_e for our sample of strong lenses. The solid line shows the power-law fit (equation 1), and the shaded region indicates the 1σ range. For reference, we show the projected stellar mass profile for the Salpeter IMF as the dotted line.

profile, $\rho(r) \propto r^\gamma$. Following Rusin, Kochanek, & Keeton (2003), in what follows we take account of the diversity of individual lens systems by uniformly rescaling the estimated errors by a constant factor so that the best-fit model has $\chi^2/N_{\rm dof} = 1$, where $N_{\rm dof}$ is the number of degrees of freedom. We find the best-fit slope of $\gamma = -2.11 \pm 0.05$, which is slightly steeper than the singular isothermal profile ($\gamma = -2$). Our result is consistent with earlier attempts by Rusin, Kochanek, & Keeton (2003) and Rusin & Kochanek (2005), and also with the combined lensing and kinematics constraints (Koopmans et al. 2009; Auger et al. 2010b; Bolton et al. 2012).

3.2 The IMF-$f_{\rm DM}$ degeneracy

We now want to decompose the stellar and dark matter distributions. However there is a fundamental difficulty in this decomposition, because of the well-known degeneracy between the relative contributions of stellar and dark matter. This can be understood very easily; all the observed lensing and kinematics data should be explained by dark matter only, without adding any contributions from stellar masses, as long as the assumed dark matter distribution is flexible enough. This indicates that IMF models that predict very small stellar masses cannot be excluded if we allow enough dark matter in galaxy cores to explain lensing and kinematics data, suggesting a fundamental degeneracy between the IMF and the dark matter fraction $f_{\rm DM}$. Hereafter we refer to it as the IMF-$f_{\rm DM}$ degeneracy.

How can we break the IMF-$f_{\rm DM}$ degeneracy? The traditional approach is to add priors on the dark matter distribution (e.g., Treu et al. 2010; Auger et al. 2010a; Dutton et al. 2011; Cappellari et al. 2012; Sonnenfeld et al. 2012) and the population of dark haloes (Dutton et al. 2013). For instance, the dark matter distribution is often assumed to follow the NFW profile or the NFW profile modified by the so-called adiabatic contraction (Blumenthal et al. 1986; Gnedin et al.

2004; Abadi et al. 2010). Sometimes it is also assumed that the contribution of dark matter is negligibly small at the core of galaxies.

Alternatively, the degeneracy is broken if we add an independent constraint on the IMF. Indeed such a constraint is available from the spectral features that are sensitive to dwarf stars (van Dokkum & Conroy 2010; Conroy & van Dokkum 2012; Ferreras et al. 2013; Conroy et al. 2013; Spiniello et al. 2013). These analyses indicate that the IMF of massive elliptical galaxies tends to have a Salpeter-like "bottom-heavy" shape and disfavors Chabrier-like IMFs.

In this paper, we employ a totally different approach to break the IMF-$f_{\rm DM}$ degeneracy. The idea is to add constraints from quasar microlensing which directly measures the fraction of mass in the form of stars (stellar mass fraction) at the positions of lensed quasar images (e.g., Schechter & Wambsganss 2002; Kochanek 2004; Bate, Webster, & Wyithe 2007; Pooley et al. 2009; Mediavilla et al. 2009). Simply said, we can constrain the stellar mass fraction because the effect of microlensing is more pronounced for a higher stellar mass fraction. Thus, quasar microlensing measurements directly constrain $f_{\rm DM}$ at the projected positions of lensed quasar images and hence break the IMF-$f_{\rm DM}$ degeneracy.

Specifically we adopt X-ray microlensing measurements of 12 quasar lenses presented in Pooley et al. (2012) as well as optical microlensing measurements of 3 quasar lenses presented in Bate et al. (2011). We exclude H1413+117 in the X-ray microlensing sample of Pooley et al. (2012) from our analysis because the effective radius is not measured for this lens system. In our analysis we adopt the probability distributions of the stellar mass fraction obtained for individual lens systems and include them as constraints at radii $R_{\rm Ein}/R_e$. X-ray quasar microlensing has an advantage over optical microlensing in that the size of the X-ray emitting region is much smaller than the Einstein radii of stars (Pooley et al. 2007; Morgan et al. 2008, 2012; Chartas et al. 2009, 2012; Dai et al. 2010) and hence results are insensitive to the assumed source sizes. On the other hand, the optical microlensing results of Bate et al. (2011) involve a proper marginalization over the size of the optical emitting region. We note that the microlensing measurements of the stellar mass fraction are not very sensitive to the slope of the IMF (Wyithe & Turner 2001; Schechter, Wambsganss, & Lewis 2004; Congdon, Keeton, & Osmer 2007), and therefore we can assume that the microlensing constraints on the stellar mass fraction are independent of the IMF, at least for our range of interest.

3.3 Two Components Model

Next we consider a two-component model that consists of stellar and dark matter. The stellar matter component is modelled by the Hernquist profile (Hernquist 1990) that resembles the de Vaucouleurs profile when projected along the line-of-sight. Specifically, we model the enclosed projected mass profile of the stellar component as

$$\frac{M_{\rm ste}(< R)}{M_*^{\rm Sal}} = \alpha_{\rm SPS}^{\rm Sal} \left(\frac{R}{R_b}\right)^2 \frac{1 - F(R/R_b)}{(R/R_b)^2 - 1}, \qquad (2)$$
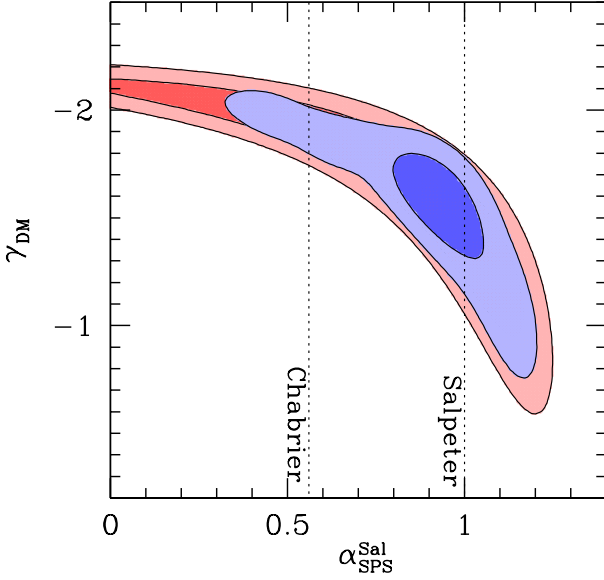
Figure 3. Projected constraints in the $\alpha_{\rm SPS}^{\rm Sal}$-$\gamma_{\rm DM}$ plane for the two-component model. Outer (*red*) contours show 1 and 2σ contours without adding the microlensing constraints (see Section 3.2), whereas the inner (*blue*) contours show the constraints including the microlensing constraints. Values of $\alpha_{\rm SPS}^{\rm Sal}$ corresponding to the Salpeter and Chabrier IMFs are indicated by vertical dotted lines.

$$
F(u) = \frac{1}{\sqrt{1-u^2}}\mathrm{arctanh}\sqrt{1-u^2} \quad (u<1), \tag{3}
$$

$$
= \frac{1}{\sqrt{u^2-1}}\arctan\sqrt{u^2-1} \quad (u>1). \tag{4}
$$

with $R_b = 0.551 R_e$. The parameter $\alpha_{\rm SPS}^{\rm Sal}$ takes account of the uncertainty of the IMF; $\alpha_{\rm SPS}^{\rm Sal} = 1$ means that the IMF is described by the Salpeter IMF, whereas $\alpha_{\rm SPS}^{\rm Sal} \approx 0.56$ corresponds to the Chabrier IMF. On the other hand, we assume a simple power-law mass distribution for the dark matter distribution

$$
\frac{M_{\rm DM}(<R)}{M_*^{\rm Sal}} = A_{\rm DM}\left(\frac{R}{R_e}\right)^{3+\gamma_{\rm DM}}. \tag{5}
$$

The total mass distribution is simply given by the sum of these two components

$$
\frac{M_{\rm tot}(<R)}{M_*^{\rm Sal}} = \frac{M_{\rm ste}(<R)}{M_*^{\rm Sal}} + \frac{M_{\rm DM}(<R)}{M_*^{\rm Sal}}. \tag{6}
$$

Thus the two-component model has 3 parameters, $\alpha_{\rm SPS}^{\rm Sal}$, $A_{\rm DM}$, and $\gamma_{\rm DM}$.

Figures 3 and 4 show projected constraints in the $\alpha_{\rm SPS}^{\rm Sal}$-$\gamma_{\rm DM}$ and $A_{\rm DM}$-$\gamma_{\rm DM}$ planes, respectively. Without the microlensing constraints (see Section 3.2 for details), the constraints are quite degenerate such that models with $\alpha_{\rm SPS}^{\rm Sal} \approx 0$ are allowed. Our result indicates that the quasar microlensing measurements of the stellar mass fraction indeed break the IMF-$f_{\rm DM}$ degeneracy. The best-fit parameters are $\alpha_{\rm SPS}^{\rm Sal} = 0.92^{+0.09}_{-0.08}$, $\gamma_{\rm DM} = -1.60^{+0.18}_{-0.13}$, and $A_{\rm DM} = M_{\rm DM}(<R_e)/M_*^{\rm Sal} = 0.21 \pm 0.04$. The Salpeter IMF is preferred over the Chabrier IMF, which is in line with recent claims based on subtle spectral features (van Dokkum & Conroy 2010; Conroy & van Dokkum 2012; Ferreras et al. 2013;
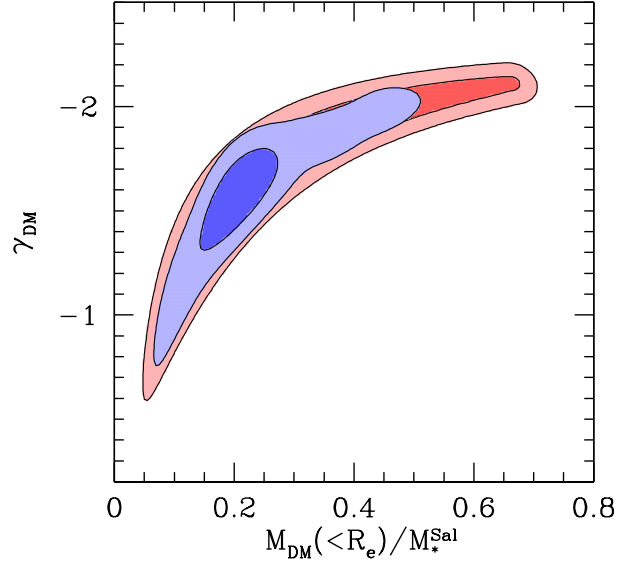
Figure 4. Similar to Figure 3, but the projected constraints in the $A_{\rm DM} = M_{\rm DM}(<R_e)/M_*^{\rm Sal}$-$\gamma_{\rm DM}$ plane are shown.
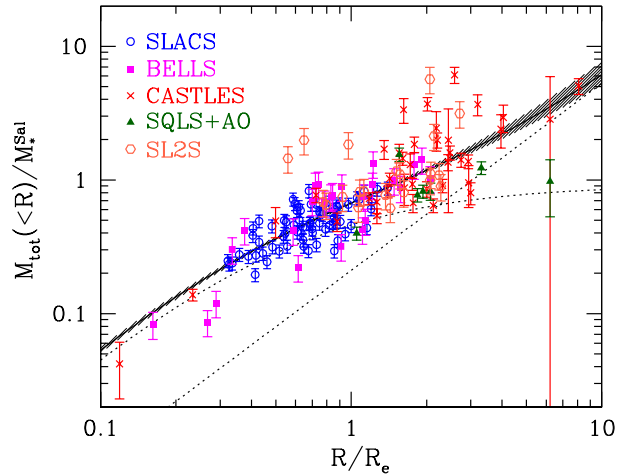
Figure 5. Similar to Figure 5, but the best-fit two-component model is overplotted. The solid line with shading shows the best-fit and 1σ range of the total mass profile. Dotted lines indicate best-fit stellar and dark matter distributions.

Conroy et al. 2013; Spiniello et al. 2013, but see also Ferreras, Saha, & Burles 2008; Ferreras et al. 2010; Smith & Lucey 2013). In addition, we find that models without dark matter ($A_{\rm DM} = 0$) are disfavored at the 5σ level even without the microlensing constraints. The best-fit two component model is shown in Figure 5.

3.4 Mass and Redshift Dependences

There have been several indications from recent lensing and/or kinematics studies (Treu et al. 2010; Dutton et al. 2011; Dutton, Mendel, & Simard 2012; Cappellari et al. 2012) as well as from studies of spectral features (van Dokkum & Conroy 2010; Conroy & van Dokkum 2012; Ferreras et al. 2013; Conroy et al. 2013;

Spiniello et al. 2013) that the IMF is non-universal, i.e., the IMF changes with galaxy velocity dispersions and stellar masses. Some previous studies from combined lensing kinematics analyses have also indicated possible redshift evolution of the slope of the total mass profile (Ruff et al. 2011; Bolton et al. 2012; Sonnenfeld et al. 2013b).

Here we investigate whether the total mass profile measured from the ensemble of strong lenses depends on the stellar mass or the redshift. We divide our strong lens sample into subsamples of different stellar mass or redshift bins to see how the fitting parameters change with these parameters. Specifically, we consider two stellar mass bins divided at $M_*^{\rm Sal} = 3 \times 10^{11} M_\odot$ and two redshift bins divided at $z_l = 0.4$. For each subsample we repeat the power-law fit to the total mass profile as presented in Section 3.1, and derive constraints on the mass normalization A and the radial slope γ in equation (1).

Figure 6 shows constraints in the $A = M_{\rm tot}(< R_e)/M_*^{\rm Sal}$-$\gamma$ plane. We find trends of the best-fit values, such that the higher stellar mass sample prefers steeper radial slope, and higher redshift sample prefers larger normalization of the total mass profile. One possible interpretation of the dependence on the stellar mass is that the lower stellar mass sample has a larger satellite fraction and therefore effectively shallower radial density slope. The larger mass normalization for the higher redshift sample can be due to either a larger dark matter fraction or a larger stellar mass (i.e., larger $\alpha_{\rm SPS}^{\rm Sal}$). The larger dark matter fraction at higher redshift may be explained by star formation in these galaxies or infall of satellite galaxies via dynamical friction. We note however that these trends with the stellar mass and redshift are not very significant, at $\lesssim 2\sigma$ level. Improved statistical analysis with a significantly larger sample of strong gravitational lenses is necessary for more detailed studies.

4   IMPLICATIONS FOR THE ADIABATIC CONTRACTION

Our measurements of the average dark matter distribution at the core of elliptical galaxies enable a direct test of models of the modification of the dark matter density profile due to baryonic physics. The most popular model of such a baryonic effect has been the adiabatic contraction (Blumenthal et al. 1986; Gnedin et al. 2004; Abadi et al. 2010) which predicts that the dissipative collapse of baryons leads to a more centrally concentrated dark matter distribution as compared with what we would expect for the case of no baryons.

Here we compute the expected dark matter distribution for our sample of strong lenses, as follows. We employ the stellar mass-dark halo relation derived in Leauthaud et al. (2012) in which the relation has been constrained up to $z \sim 1$ from lensing and clustering observations. We note that Leauthaud et al. (2012) assumed the Chabrier IMF for computing the stellar mass, and thus $M_*^{\rm Sal}$ for our lens sample is first converted to stellar mass with the Chabrier IMF by multiplying by 0.56 before applying the stellar mass-dark halo relation in Leauthaud et al. (2012) to compute the halo mass for each lens system. We adopt the mass-concentration relation of Duffy et al. (2008) to compute the concentration parameter. We add a log-normal scatter of 0.2 dex for the concentration parameter, the baryon mass fraction, and the
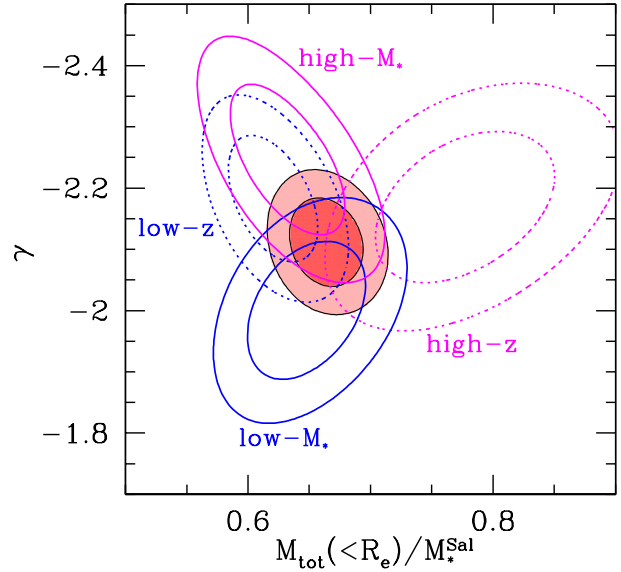
Figure 6. Constraints in the $A = M_{\rm tot}(< R_e)/M_*^{\rm Sal}$-$\gamma$ plane for the power-law model (see Section 3.1). Filled contours show 1 and 2σ contours from the full strong lens sample. Contours with solid lines show 1 and 2σ contours from subsamples with stellar mass $M_*^{\rm Sal}$ larger or smaller than $3 \times 10^{11} M_\odot$. Contours with dotted lines show 1 and 2σ contours from subsamples with redshift lower or higher than 0.4.
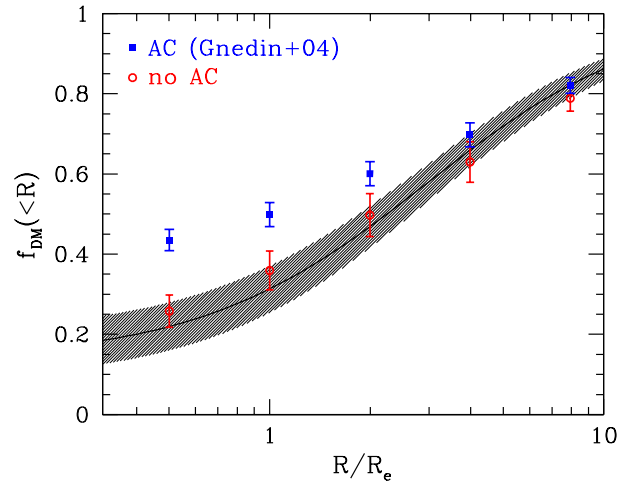
Figure 7. The dark matter fraction within the projected radius R. The solid line with shading shows the dark matter fraction from the best-fit two component model. Filled squares with errors indicate expected dark matter fraction for the adiabatic contraction model of Gnedin et al. (2004). Open circles with errors show the expected dark matter fraction for the NFW profile without adiabatic contraction.

scale radius. Again we assume the Hernquist model for the baryon mass distribution. We assume that the dark matter distribution is modified from the NFW profile by the adiabatic contraction model of Gnedin et al. (2004) who derived a fitting formula of the adiabatic contraction based on high-resolution hydrodynamical simulations. For comparison, we consider a dark matter model of the pure NFW profile without the adiabatic contraction.

Figure 7 compares the dark matter fractions at several different radii for the best-fit two component model with the model predictions described above. We find that the adiabatic contraction model of Gnedin et al. (2004) overpredicts the dark matter fraction at $R \lesssim 2R_e$. The observed dark matter fraction is more consistent with the NFW model without the adiabatic contraction.

Our result is in line with recent studies with lensing and stellar kinematics which prefer moderate or no adiabatic contraction (e.g., Auger et al. 2010a; Dutton et al. 2013; Newman et al. 2013b), and suggests other physical process may also play an important role. For instance, dissipationless mergers of stellar clumps can indeed decrease the central dark matter density as compared with the one predicted by adiabatic contraction (e.g., Naab et al. 2007; Lackner & Ostriker 2010). Dissipationless mergers appear to be consistent with the possible redshift evolution of the dark matter fraction as discussed in Section 3.4.

5 SUMMARY

We have studied the average mass distribution of elliptical galaxies with the statistical analysis of 161 strong gravitational lens systems compiled from several surveys. Each strong lens system provides a robust measurement of the enclosed mass within the Einstein radius, and hence assuming that the mass distribution scales with the stellar mass and the effective radius we can reconstruct the total mass distribution. When fitted to a single power-law, the total mass profile is described by $\rho(r) \propto r^{\gamma}$ with the best-fit slope of $\gamma = -2.11 \pm 0.05$. We have argued that the decomposition of the total mass profile into the stellar and dark matter distribution involves a fundamental difficulty due to the IMF-$f_{\rm DM}$ degeneracy, which is very difficult to break if we assume flexible enough dark matter distribution. We have demonstrated that the IMF-$f_{\rm DM}$ degeneracy can be broken by adding quasar microlensing constraints which directly measure the stellar mass fraction at the positions of quasar images. Our best-fit model favors the Salpeter IMF over the Chabrier IMF and the best-fit dark matter density slope of $\gamma_{\rm DM} = -1.60^{+0.18}_{-0.13}$. The inclusion of dark matter component is required at the 5σ level. We find some possible trends of the total density profile with the stellar mass and redshift. Finally, we have compared the observed dark matter fraction with predicted dark matter fractions with and without the adiabatic contraction and found that the model without adiabatic contraction better explains the result.

These results are obtained using gravitational lensing only without relying on the stellar kinematics data. Our results are generally in agreement with results using the stellar kinematics information, in which nearly isotropic velocity dispersion near the galaxy center is assumed. This suggests that the velocity anisotropy is indeed small, although careful combined analysis will be necessary to assess the degree of the velocity anisotropy more quantitatively.

A more comprehensive analysis of dependences of the stellar and dark matter distributions will benefit from a larger sample of galaxy scale strong gravitational lenses, which will be obtained in future wide-field imaging surveys (e.g., Oguri & Marshall 2010). Large samples of strong lenses are being constructed from bright submillimeter galaxies (Negrello et al. 2010; González-Nuevo et al. 2012; Vieira et al. 2013; Bussmann et al. 2013), which should significantly advance various statistical analyses of strong gravitational lenses as the one presented in this paper. Measurements of quasar microlensing for more quasar lens systems are also important to map the dark matter content of galaxies accurately.

REFERENCES

Abadi M. G., Navarro J. F., Fardal M., Babul A., Steinmetz M., 2010, MNRAS, 407, 435
Anguita T., Faure C., Kneib J.-P., Wambsganss J., Knobel C., Koekemoer A. M., Limousin M., 2009, A&A, 507, 35
Auger M. W., Treu T., Bolton A. S., Gavazzi R., Koopmans L. V. E., Marshall P. J., Bundy K., Moustakas L. A., 2009, ApJ, 705, 1099
Auger M. W., Treu T., Gavazzi R., Bolton A. S., Koopmans L. V. E., Marshall P. J., 2010a, ApJ, 721, L163
Auger M. W., Treu T., Bolton A. S., Gavazzi R., Koopmans L. V. E., Marshall P. J., Moustakas L. A., Burles S., 2010b, ApJ, 724, 511
Bacon R., et al., 2001, MNRAS, 326, 23
Bate N. F., Webster R. L., Wyithe J. S. B., 2007, MNRAS, 381, 1591
Bate N. F., Floyd D. J. E., Webster R. L., Wyithe J. S. B., 2011, ApJ, 731, 71
Binney J., Tremaine S., 2008, gady.book,
Blumenthal G. R., Faber S. M., Flores R., Primack J. R., 1986, ApJ, 301, 27
Bolton A. S., Burles S., Koopmans L. V. E., Treu T., Moustakas L. A., 2006, ApJ, 638, 703
Bolton A. S., Burles S., Koopmans L. V. E., Treu T., Gavazzi R., Moustakas L. A., Wayth R., Schlegel D. J., 2008a, ApJ, 682, 964
Bolton A. S., Treu T., Koopmans L. V. E., Gavazzi R., Moustakas L. A., Burles S., Schlegel D. J., Wayth R., 2008b, ApJ, 684, 248
Bolton A. S., et al., 2012, ApJ, 757, 82
Brownstein J. R., et al., 2012, ApJ, 744, 41
Bruzual G., Charlot S., 2003, MNRAS, 344, 1000
Bussmann R. S., et al., 2013, arXiv, arXiv:1309.0836
Cabanac R. A., et al., 2007, A&A, 461, 813
Cappellari M., et al., 2006, MNRAS, 366, 1126
Cappellari M., et al., 2007, MNRAS, 379, 418
Cappellari M., et al., 2011, MNRAS, 413, 813
Cappellari M., et al., 2012, Natur, 484, 485
Cappellari M., et al., 2013a, MNRAS, 432, 1709
Cappellari M., et al., 2013b, MNRAS, 432, 1862
Chabrier G., 2003, PASP, 115, 763

Chartas G., Kochanek C. S., Dai X., Poindexter S., Garmire G., 2009, ApJ, 693, 174

Chartas G., Kochanek C. S., Dai X., Moore D., Mosquera A. M., Blackburne J. A., 2012, ApJ, 757, 137

Congdon A. B., Keeton C. R., Osmer S. J., 2007, MNRAS, 376, 263

Conroy C., van Dokkum P. G., 2012, ApJ, 760, 71

Conroy C., Dutton A. A., Graves G. J., Mendel J. T., van Dokkum P. G., 2013, arXiv, arXiv:1306.2316

Dai X., Kochanek C. S., Chartas G., Kozłowski S., Morgan C. W., Garmire G., Agol E., 2010, ApJ, 709, 278

Duffy A. R., Schaye J., Kay S. T., Dalla Vecchia C., 2008, MNRAS, 390, L64

Dutton A. A., et al., 2011, MNRAS, 416, 322

Dutton A. A., Mendel J. T., Simard L., 2012, MNRAS, 422, L33

Dutton A. A., et al., 2013, MNRAS, 428, 3183

Ferreras I., La Barbera F., de la Rosa I. G., Vazdekis A., de Carvalho R. R., Falcón-Barroso J., Ricciardelli E., 2013, MNRAS, 429, L15

Ferreras I., Saha P., Leier D., Courbin F., Falco E. E., 2010, MNRAS, 409, L30

Ferreras I., Saha P., Burles S., 2008, MNRAS, 383, 857

Ferreras I., Saha P., Williams L. L. R., 2005, ApJ, 623, L5

Gavazzi R., Treu T., Rhodes J. D., Koopmans L. V. E., Bolton A. S., Burles S., Massey R. J., Moustakas L. A., 2007, ApJ, 667, 176

Gavazzi R., Treu T., Marshall P. J., Brault F., Ruff A., 2012, ApJ, 761, 170

Gnedin O. Y., Kravtsov A. V., Klypin A. A., Nagai D., 2004, ApJ, 616, 16

González-Nuevo J., et al., 2012, ApJ, 749, 65

Grillo C., 2010, ApJ, 722, 779

Grillo C., 2012, ApJ, 747, L15

Hayano Y., et al., 2008, SPIE, 7015, 701510

Hayano Y., et al., 2010, SPIE, 7736, 77360N

Hernquist L., 1990, ApJ, 356, 359

Hoekstra H., Yee H. K. C., Gladders M. D., 2004, ApJ, 606, 67

Inada N., et al., 2008, AJ, 135, 496

Inada N., et al., 2010, AJ, 140, 403

Inada N., et al., 2012, AJ, 143, 119

Johnston D. E., et al., 2007, arXiv, arXiv:0709.1159

Kochanek C. S., 2004, ApJ, 605, 58

Koopmans L. V. E., et al., 2009, ApJ, 703, L51

Krajnović D., et al., 2011, MNRAS, 414, 2923

Kroupa P., 2001, MNRAS, 322, 231

Kuntschner H., et al., 2010, MNRAS, 408, 97

Lackner C. N., Ostriker J. P., 2010, ApJ, 712, 88

Leauthaud A., et al., 2012, ApJ, 744, 159

Mandelbaum R., Seljak U., Cool R. J., Blanton M., Hirata C. M., Brinkmann J., 2006, MNRAS, 372, 758

Mandelbaum R., Seljak U., Hirata C. M., 2008, JCAP, 8, 6

Mediavilla E., et al., 2009, ApJ, 706, 1451

More A., Cabanac R., More S., Alard C., Limousin M., Kneib J.-P., Gavazzi R., Motta V., 2012, ApJ, 749, 38

Morgan C. W., Kochanek C. S., Dai X., Morgan N. D., Falco E. E., 2008, ApJ, 689, 755

Morgan C. W., et al., 2012, ApJ, 756, 52

Naab T., Johansson P. H., Ostriker J. P., Efstathiou G., 2007, ApJ, 658, 710

Navarro J. F., Frenk C. S., White S. D. M., 1997, ApJ, 490, 493

Negrello M., et al., 2010, Sci, 330, 800

Newman A. B., Treu T., Ellis R. S., Sand D. J., Nipoti C., Richard J., Jullo E., 2013a, ApJ, 765, 24

Newman A. B., Treu T., Ellis R. S., Sand D. J., 2013b, ApJ, 765, 25

Oguri M., 2010, PASJ, 62, 1017

Oguri M., Marshall P. J., 2010, MNRAS, 405, 2579

Oguri M., Bayliss M. B., Dahle H., Sharon K., Gladders M. D., Natarajan P., Hennawi J. F., Koester B. P., 2012a, MNRAS, 420, 3213

Oguri M., et al., 2006, AJ, 132, 999

Oguri M., et al., 2008, AJ, 135, 512

Oguri M., et al., 2012b, AJ, 143, 120

Okabe N., Smith G. P., Umetsu K., Takada M., Futamase T., 2013, ApJ, 769, L35

Pooley D., Blackburne J. A., Rappaport S., Schechter P. L., 2007, ApJ, 661, 19

Pooley D., Rappaport S., Blackburne J., Schechter P. L., Schwab J., Wambsganss J., 2009, ApJ, 697, 1892

Pooley D., Rappaport S., Blackburne J. A., Schechter P. L., Wambsganss J., 2012, ApJ, 744, 111

Ruff A. J., Gavazzi R., Marshall P. J., Treu T., Auger M. W., Brault F., 2011, ApJ, 727, 96

Rusin D., Kochanek C. S., Keeton C. R., 2003, ApJ, 595, 29

Rusin D., Kochanek C. S., 2005, ApJ, 623, 666

Rusu C. E., et al., 2011, ApJ, 738, 30

Salpeter E. E., 1955, ApJ, 121, 161

Schechter P. L., Wambsganss J., 2002, ApJ, 580, 685

Schechter P. L., Wambsganss J., Lewis G. F., 2004, ApJ, 613, 77

Sluse D., Courbin F., Eigenbrod A., Meylan G., 2008, A&A, 492, L39

Smith R. J., Lucey J. R., 2013, MNRAS, 434, 1964

Sonnenfeld A., Treu T., Gavazzi R., Marshall P. J., Auger M. W., Suyu S. H., Koopmans L. V. E., Bolton A. S., 2012, ApJ, 752, 163

Sonnenfeld A., Gavazzi R., Suyu S. H., Treu T., Marshall P. J., 2013a, arXiv, arXiv:1307.4764

Sonnenfeld A., Treu T., Gavazzi R., Suyu S. H., Marshall P. J., Auger M. W., Nipoti C., 2013b, arXiv, arXiv:1307.4759

Spiniello C., Trager S., Koopmans L. V. E., Conroy C., 2013, arXiv, arXiv:1305.2873

Treu T., Auger M. W., Koopmans L. V. E., Gavazzi R., Marshall P. J., Bolton A. S., 2010, ApJ, 709, 1195

Treu T., 2010, ARA&A, 48, 87

Treu T., Koopmans L. V. E., 2002, ApJ, 575, 87

Treu T., Koopmans L. V. E., 2004, ApJ, 611, 739

Treu T., Dutton A. A., Auger M. W., Marshall P. J., Bolton A. S., Brewer B. J., Koo D. C., Koopmans L. V. E., 2011, MNRAS, 417, 1601

van Dokkum P. G., Conroy C., 2010, Natur, 468, 940

Vieira J. D., et al., 2013, Natur, 495, 344

Umetsu K., Broadhurst T., Zitrin A., Medezinski E., Coe D., Postman M., 2011, ApJ, 738, 41

Wambsganss J., 2006, glsw.conf, 453

Wyithe J. S. B., Turner E. L., 2001, MNRAS, 320, 21

APPENDIX A: LIST OF STRONG GRAVITATIONAL LENSES

Table A1 shows a list of all 161 strong gravitational lens systems used in this paper.

Table A1: List of 161 strong gravitational lens systems used for the statistical analysis. For each strong lens system we show the lens redshift z_l, the source redshift (z_s), the effective radius measured at the intermediate axis (θ_e), the stellar mass assuming the Salpeter IMF $(\log M_*^{\text{Sal}})$, and the Einstein radius (θ_{Ein}).

Name	Sample	z_l	z_s	θ_e (arcsec)	$\log M_*^{\text{Sal}}$ $(M_\odot)$	θ_{Ein} (arcsec)
SDSSJ0008−0004	SLACS	0.440	1.192	1.71 ± 0.09	11.63	1.16
SDSSJ0029−0055	SLACS	0.227	0.931	2.16 ± 0.11	11.63	0.96
SDSSJ0037−0942	SLACS	0.195	0.632	1.80 ± 0.09	11.79	1.53
SDSSJ0044+0113	SLACS	0.120	0.197	1.92 ± 0.10	11.53	0.80
SDSSJ0157−0056	SLACS	0.513	0.924	1.84 ± 0.09	11.72	0.79
SDSSJ0216−0813	SLACS	0.332	0.523	2.40 ± 0.12	12.04	1.16
SDSSJ0252+0039	SLACS	0.280	0.982	1.39 ± 0.07	11.49	1.04
SDSSJ0330−0020	SLACS	0.351	1.071	0.91 ± 0.05	11.57	1.10
SDSSJ0728+3835	SLACS	0.206	0.688	1.78 ± 0.09	11.70	1.25
SDSSJ0737+3216	SLACS	0.322	0.581	1.80 ± 0.09	11.96	1.00
SDSSJ0819+4534	SLACS	0.194	0.446	1.98 ± 0.10	11.51	0.85
SDSSJ0822+2652	SLACS	0.241	0.594	1.82 ± 0.09	11.73	1.17
SDSSJ0841+3824	SLACS	0.116	0.657	4.21 ± 0.21	11.75	1.41
SDSSJ0903+4116	SLACS	0.430	1.065	1.78 ± 0.09	11.84	1.29
SDSSJ0912+0029	SLACS	0.164	0.324	4.01 ± 0.20	11.96	1.63
SDSSJ0935−0003	SLACS	0.347	0.467	2.15 ± 0.11	12.02	0.87
SDSSJ0936+0913	SLACS	0.190	0.588	2.11 ± 0.11	11.71	1.09
SDSSJ0946+1006	SLACS	0.222	0.609	2.35 ± 0.12	11.61	1.38
SDSSJ0955+0101	SLACS	0.111	0.316	1.47 ± 0.07	11.03	0.91
SDSSJ0956+5100	SLACS	0.241	0.470	2.19 ± 0.11	11.80	1.33
SDSSJ0959+4416	SLACS	0.237	0.531	1.98 ± 0.10	11.73	0.96
SDSSJ0959+0410	SLACS	0.126	0.535	1.29 ± 0.06	11.14	0.99
SDSSJ1016+3859	SLACS	0.168	0.439	1.46 ± 0.07	11.49	1.09
SDSSJ1020+1122	SLACS	0.282	0.553	1.59 ± 0.08	11.79	1.20
SDSSJ1023+4230	SLACS	0.191	0.696	1.77 ± 0.09	11.58	1.41
SDSSJ1029+0420	SLACS	0.104	0.615	1.56 ± 0.08	11.28	1.01
SDSSJ1032+5322	SLACS	0.133	0.329	0.81 ± 0.04	11.11	1.03
SDSSJ1100+5329	SLACS	0.317	0.858	2.20 ± 0.11	11.86	1.52
SDSSJ1103+5322	SLACS	0.158	0.735	2.85 ± 0.14	11.54	1.02
SDSSJ1106+5228	SLACS	0.095	0.407	1.39 ± 0.07	11.41	1.23
SDSSJ1112+0826	SLACS	0.273	0.629	1.32 ± 0.07	11.74	1.49
SDSSJ1134+6027	SLACS	0.153	0.474	2.02 ± 0.10	11.50	1.10
SDSSJ1142+1001	SLACS	0.222	0.504	1.24 ± 0.06	11.59	0.98
SDSSJ1143−0144	SLACS	0.106	0.402	2.66 ± 0.13	11.68	1.68
SDSSJ1153+4612	SLACS	0.180	0.875	1.16 ± 0.06	11.36	1.05
SDSSJ1204+0358	SLACS	0.164	0.631	1.09 ± 0.05	11.45	1.31
SDSSJ1205+4910	SLACS	0.215	0.481	1.79 ± 0.09	11.73	1.22
SDSSJ1213+6708	SLACS	0.123	0.640	1.50 ± 0.08	11.57	1.42
SDSSJ1218+0830	SLACS	0.135	0.717	2.70 ± 0.14	11.64	1.45
SDSSJ1250+0523	SLACS	0.232	0.795	1.32 ± 0.07	11.79	1.13
SDSSJ1251−0208	SLACS	0.224	0.784	2.61 ± 0.13	11.59	0.84
SDSSJ1306+0600	SLACS	0.173	0.472	1.25 ± 0.06	11.47	1.32
SDSSJ1313+4615	SLACS	0.185	0.514	1.59 ± 0.08	11.61	1.37
SDSSJ1318−0313	SLACS	0.240	1.300	2.51 ± 0.13	11.73	1.58
SDSSJ1330−0148	SLACS	0.081	0.711	0.96 ± 0.05	10.70	0.86
SDSSJ1402+6321	SLACS	0.205	0.481	2.29 ± 0.11	11.79	1.35
SDSSJ1403+0006	SLACS	0.189	0.473	1.14 ± 0.06	11.47	0.83
SDSSJ1416+5136	SLACS	0.299	0.811	0.98 ± 0.05	11.63	1.37
SDSSJ1420+6019	SLACS	0.063	0.535	2.25 ± 0.11	11.20	1.04
SDSSJ1430+4105	SLACS	0.285	0.575	2.55 ± 0.13	11.91	1.52
SDSSJ1432+6317	SLACS	0.123	0.664	3.04 ± 0.15	11.76	1.26
SDSSJ1436−0000	SLACS	0.285	0.805	1.63 ± 0.08	11.68	1.12
SDSSJ1443+0304	SLACS	0.134	0.419	0.70 ± 0.03	11.14	0.81

Table A1 continued

Name	Sample	z_l	z_s	θ_e (arcsec)	$\log M_*^{\text{Sal}}$ ($M_\odot$)	θ_{Ein} (arcsec)
SDSSJ1451−0239	SLACS	0.125	0.520	1.54 ± 0.08	11.45	1.04
SDSSJ1525+3327	SLACS	0.358	0.717	2.42 ± 0.12	11.99	1.31
SDSSJ1531−0105	SLACS	0.160	0.744	1.97 ± 0.10	11.75	1.71
SDSSJ1538+5817	SLACS	0.143	0.531	1.00 ± 0.05	11.30	1.00
SDSSJ1614+4522	SLACS	0.178	0.811	2.58 ± 0.13	11.49	0.84
SDSSJ1621+3931	SLACS	0.245	0.602	1.51 ± 0.08	11.75	1.29
SDSSJ1627−0053	SLACS	0.208	0.524	1.98 ± 0.10	11.66	1.23
SDSSJ1630+4520	SLACS	0.248	0.793	1.65 ± 0.08	11.83	1.78
SDSSJ1636+4707	SLACS	0.228	0.675	1.68 ± 0.08	11.69	1.08
SDSSJ1644+2625	SLACS	0.137	0.610	1.55 ± 0.08	11.46	1.27
SDSSJ1719+2939	SLACS	0.181	0.578	1.46 ± 0.07	11.48	1.28
SDSSJ2238−0754	SLACS	0.137	0.713	1.82 ± 0.09	11.47	1.27
SDSSJ2300+0022	SLACS	0.228	0.463	1.52 ± 0.08	11.64	1.24
SDSSJ2303+1422	SLACS	0.155	0.517	2.94 ± 0.15	11.74	1.62
SDSSJ2321−0939	SLACS	0.082	0.532	4.11 ± 0.21	11.66	1.60
SDSSJ2341+0000	SLACS	0.186	0.807	2.36 ± 0.12	11.74	1.44
SDSSJ2347−0005	SLACS	0.417	0.714	1.14 ± 0.06	11.85	1.11
SDSSJ0151+0049	BELLS	0.517	1.364	0.67 ± 0.07	11.35	0.75
SDSSJ0747+5055	BELLS	0.438	0.898	1.09 ± 0.11	11.50	0.64
SDSSJ0747+4448	BELLS	0.437	0.897	0.92 ± 0.09	11.39	0.72
SDSSJ0801+4727	BELLS	0.483	1.518	0.50 ± 0.05	11.20	0.89
SDSSJ0830+5116	BELLS	0.530	1.332	0.97 ± 0.10	11.44	0.89
SDSSJ0944−0147	BELLS	0.539	1.179	0.48 ± 0.05	11.32	0.92
SDSSJ1159−0007	BELLS	0.579	1.346	0.96 ± 0.10	11.48	0.81
SDSSJ1215+0047	BELLS	0.642	1.297	0.65 ± 0.07	11.67	0.74
SDSSJ1221+3806	BELLS	0.535	1.284	0.47 ± 0.05	11.31	0.74
SDSSJ1234−0241	BELLS	0.490	1.016	1.05 ± 0.11	11.50	0.28
SDSSJ1318−0104	BELLS	0.659	1.396	0.69 ± 0.07	11.50	0.84
SDSSJ1337+3620	BELLS	0.564	1.182	2.03 ± 0.20	11.76	0.68
SDSSJ1349+3612	BELLS	0.440	0.893	1.89 ± 0.19	11.59	0.71
SDSSJ1352+3216	BELLS	0.463	1.034	0.58 ± 0.06	11.37	0.86
SDSSJ1522+2910	BELLS	0.555	1.311	0.89 ± 0.09	11.39	0.74
SDSSJ1541+1812	BELLS	0.560	1.113	0.76 ± 0.08	11.41	0.93
SDSSJ1542+1629	BELLS	0.352	1.023	0.73 ± 0.07	11.52	0.81
SDSSJ1545+2748	BELLS	0.522	1.289	2.59 ± 0.26	11.82	0.42
SDSSJ1601+2138	BELLS	0.543	1.446	0.44 ± 0.04	11.40	0.91
SDSSJ1611+1705	BELLS	0.477	1.211	1.00 ± 0.10	11.23	0.74
SDSSJ1631+1854	BELLS	0.408	1.086	1.43 ± 0.14	11.94	0.88
SDSSJ1637+1439	BELLS	0.391	0.874	1.04 ± 0.10	11.22	0.75
SDSSJ2122+0409	BELLS	0.626	1.452	0.90 ± 0.09	11.33	0.63
SDSSJ2125+0411	BELLS	0.363	0.978	0.90 ± 0.09	11.68	0.82
SDSSJ2303+0037	BELLS	0.458	0.936	1.35 ± 0.14	11.62	0.39
HE0047−1756	CASTLES	0.408	1.670	0.49 ± 0.12	11.18	0.80
Q0142−100	CASTLES	0.491	2.719	0.51 ± 0.03	11.53	1.18
QJ0158−4325	CASTLES	0.317	1.294	0.66 ± 0.08	11.07	0.58
HE0230−2130	CASTLES	0.522	2.162	0.14 ± 0.15	10.82	0.87
SDSSJ0246−0825	CASTLES	0.723	1.686	0.18 ± 0.06	11.08	0.53
MG0414+0534	CASTLES	0.958	2.639	0.78 ± 0.02	11.72	1.11
HE0435−1223	CASTLES	0.454	1.689	0.76 ± 0.04	11.38	1.22
B0712+472	CASTLES	0.406	1.339	0.36 ± 0.03	11.13	0.72
MG0751+2716	CASTLES	0.350	3.200	0.31 ± 0.04	10.22	0.42
HS0818+1227	CASTLES	0.390	3.115	0.62 ± 0.05	11.22	1.37
B0850+054	CASTLES	0.588	3.930	0.16 ± 0.01	10.64	0.34
SDSSJ0924+0219	CASTLES	0.393	1.523	0.30 ± 0.02	11.06	0.88
LBQS1009−0252	CASTLES	0.871	2.739	0.19 ± 0.04	10.89	0.77
J1004+1229	CASTLES	0.950	2.640	0.34 ± 0.24	11.17	0.83
B1030+074	CASTLES	0.599	1.535	0.23 ± 0.06	11.07	0.91
HE1104−1805	CASTLES	0.729	2.303	0.64 ± 0.20	11.44	1.40

Table A1 continued

Name	Sample	z_l	z_s	θ_e (arcsec)	$\log M_*^{\mathrm{Sal}}$ ($M_\odot$)	θ_{Ein} (arcsec)
PG1115+080	CASTLES	0.311	1.736	0.46 ± 0.03	11.10	1.14
RXJ1131−1231	CASTLES	0.295	0.658	1.13 ± 0.21	11.34	1.83
SDSSJ1138+0314	CASTLES	0.445	2.442	0.19 ± 0.03	10.92	0.57
SDSSJ1155+6346	CASTLES	0.176	2.888	0.43 ± 0.05	10.86	0.76
SDSSJ1226−0006	CASTLES	0.517	1.126	0.45 ± 0.07	11.21	0.57
LBQS1333+0113	CASTLES	0.440	1.571	0.31 ± 0.02	11.07	0.85
Q1355−2257	CASTLES	0.702	1.373	1.24 ± 0.29	11.56	0.62
HST14113+5211	CASTLES	0.465	2.811	0.47 ± 0.04	10.90	0.84
HST14176+5226	CASTLES	0.809	3.400	0.70 ± 0.04	11.25	1.41
B1422+231	CASTLES	0.337	3.620	0.32 ± 0.03	10.83	0.78
MG1549+3047	CASTLES	0.111	1.170	0.82 ± 0.01	10.98	1.15
B1608+656	CASTLES	0.630	1.394	0.64 ± 0.05	11.67	0.81
PMNJ1632−0033	CASTLES	1.165	3.424	0.20 ± 0.03	10.71	0.64
FBQ1633+3134	CASTLES	0.684	1.518	2.93 ± 1.26	12.07	0.35
MG1654+1346	CASTLES	0.254	1.740	0.89 ± 0.02	11.29	1.05
B1938+666	CASTLES	0.881	2.059	0.69 ± 0.05	11.17	0.50
MG2016+112	CASTLES	1.004	3.273	0.22 ± 0.02	11.41	1.78
WFI2033−4723	CASTLES	0.661	1.660	0.72 ± 0.09	11.46	1.12
B2045+265	CASTLES	0.867	1.280	0.41 ± 0.04	11.16	1.06
HE2149−2745	CASTLES	0.603	2.033	0.50 ± 0.09	11.22	0.86
Q2237+030	CASTLES	0.039	1.695	3.86 ± 0.09	11.08	0.90
COSMOS5921+0638	CASTLES	0.551	3.140	0.41 ± 0.01	11.12	0.72
SDSSJ0743+2457	SQLS+AO	0.381	2.165	0.09 ± 0.04	10.77	0.56
SDSSJ0806+2006	SQLS+AO	0.573	1.538	0.23 ± 0.01	11.17	0.76
SDSSJ0819+5356	SQLS+AO	0.294	2.239	1.12 ± 0.06	11.89	2.06
SDSSJ0946+1835	SQLS+AO	0.388	4.799	0.75 ± 0.04	11.63	1.45
SDSSJ1055+4628	SQLS+AO	0.388	1.249	0.28 ± 0.03	10.95	0.58
SDSSJ1313+5151	SQLS+AO	0.194	1.877	0.57 ± 0.03	10.94	0.60
SDSSJ1620+1203	SQLS+AO	0.398	1.158	0.90 ± 0.05	11.47	1.40
SL2SJ0213−0743	SL2S	0.717	3.480	2.45 ± 0.25	11.96	2.39
SL2SJ0214−0405	SL2S	0.609	1.880	0.93 ± 0.09	11.72	1.41
SL2SJ0217−0513	SL2S	0.646	1.850	0.61 ± 0.06	11.69	1.27
SL2SJ0219−0829	SL2S	0.389	2.150	0.57 ± 0.06	11.54	1.30
SL2SJ0225−0454	SL2S	0.238	1.200	2.28 ± 0.23	11.76	1.76
SL2SJ0226−0420	SL2S	0.494	1.230	1.06 ± 0.11	11.71	1.19
SL2SJ0232−0408	SL2S	0.352	2.340	0.96 ± 0.10	11.34	1.04
SL2SJ0849−0412	SL2S	0.722	1.540	0.49 ± 0.05	11.69	1.10
SL2SJ0849−0251	SL2S	0.274	2.090	1.46 ± 0.15	11.44	1.16
SL2SJ0901−0259	SL2S	0.670	1.190	0.50 ± 0.05	10.97	1.03
SL2SJ0904−0059	SL2S	0.611	2.360	2.50 ± 0.25	11.58	1.40
SL2SJ0959+0206	SL2S	0.552	3.350	0.54 ± 0.05	11.22	0.74
SL2SJ1359+5535	SL2S	0.783	2.770	1.76 ± 0.18	11.35	1.14
SL2SJ1405+5243	SL2S	0.526	3.010	0.73 ± 0.07	11.72	1.51
SL2SJ1406+5226	SL2S	0.716	1.470	0.60 ± 0.06	11.55	0.94
SL2SJ1411+5651	SL2S	0.322	1.420	0.65 ± 0.07	11.38	0.93
SL2SJ1420+5258	SL2S	0.380	0.990	1.04 ± 0.10	11.47	0.96
SL2SJ1420+5630	SL2S	0.483	3.120	1.31 ± 0.13	11.82	1.40
SL2SJ1427+5516	SL2S	0.511	2.580	0.50 ± 0.05	11.27	0.81
SL2SJ2203+0205	SL2S	0.400	2.150	0.72 ± 0.07	11.36	1.95
SL2SJ2213−0009	SL2S	0.338	3.450	0.50 ± 0.05	10.91	1.07